

Wavelet Methods for Studying the Onset of Strong Plasma Turbulence

A. Le et al.¹ and K. Schneider²

¹*Los Alamos National Laboratory, Los Alamos, New Mexico 87545, USA*

²*I2M, Aix-Marseille Université, Marseille, France*

Abstract

Recent kinetic simulations have demonstrated that coherent current sheets dominate the energy dissipation in strong turbulence of magnetized plasma. While weak turbulence is naturally analyzed in terms of the Fourier spectrum of its wave content, the Fourier modes are not well-suited for characterizing coherent current sheets. As an alternative, wavelet bases are used here to study the onset of turbulence. Originally used to study neutral fluid turbulence, an iterative wavelet technique extracts coherent features of the flow or current density. The onset of turbulence is identified with the growth of a background of incoherent random fluctuations spread across a range of scales. The wavelet method makes no assumptions about the structure of the coherent current sheets or the underlying plasma model, and it is applied here to Kelvin-Helmholtz unstable flow-shear layers in fully kinetic, hybrid (kinetic ion/fluid electron), two-fluid, and Hall MHD simulations.

I. INTRODUCTION

In large-scale simulations of turbulent plasmas [1, 2], a majority of the energy dissipation on kinetic scales is intermittent and occurs in localized, coherent current sheets rather than through wave interactions. While the plasma waves are naturally analyzed in terms of Fourier modes, localized structures call for decompositions that reflect their localization and their multiscale properties.

Wavelets, which are localized functions in space and scale, offer the possibility to represent intermittent functions and localized structures exhibiting a large range of scales in an efficient way. The so-called ‘mother wavelet’, $\psi(x)$, which has finite energy, is the elementary building block of the wavelet transform. It is a well-localized function with fast decay at infinity and at least one vanishing moment (*i.e.*, zero mean) or more. It is also sufficiently smooth, which implies its that Fourier transform exhibits fast decay. The wavelet transform [3] decomposes a signal (*e.g.*, in time) or any field (*e.g.*, in three-dimensional space) into both space (or time) and scale (or time scale), and possibly directions (for dimensions higher than one). The range of wavelet applications is very broad, and in the following we concentrate on turbulence in fluids and plasmas.

Wavelets have been used for analyzing hydrodynamic turbulence starting in the 1990s and then extended for modeling and computing turbulent flows. For reviews we refer to [4] and [5].

Wavelet techniques have been extensively used in the context of plasma turbulence. For example they have been applied to space [6, 7] and laboratory [8] plasma turbulence. Wavelet-based density estimation techniques to improve particle-in-cell numerical schemes were introduced in [9], and a particle-in-wavelet scheme was developed for solving the Vlasov–Poisson equations directly in wavelet space [10]. Wavelet denoising has been applied for tomographic reconstruction of tokamak plasma light emission in [11]. Coherent Vorticity and Current sheet Simulation (CVCS), which applies wavelet filtering to the resistive non-ideal MHD equations, was proposed as a new model for turbulent MHD flows. It allows a reduction in the number of degrees of freedom necessary to compute the flows, while capturing the nonlinear dynamics of the flow. A recent review on wavelet transforms and their applications to MHD and plasma turbulence can be found in [12].

The aim of the present paper is to use the wavelet decomposition of turbulent flows into coherent and incoherent contributions to define a criterion that determines the onset of plasma turbulence in different unstable shear-flows triggered by the Kelvin–Helmholtz instability. To this end, high-resolution numerical simulations using different approaches, either fully kinetic, hybrid (kinetic ion/fluid electron), two-fluid, or Hall MHD, are analyzed using orthogonal wavelets.

The outline of the paper is the following: In Section II we recall Fourier and wavelet analysis and in Section III the iterative wavelet filtering is presented. The simulation set-ups are described in Section IV. Section V introduces a wavelet-based method for quantifying the transition of flows to turbulence. The method is then applied to a more complex flow in a global magnetosphere simulation in Section VI, and a summary is given in Section VII. The Appendix discusses some issues on numerical noise present in particle simulations.

II. FOURIER AND WAVELET ANALYSIS

We review here a few concepts related to Fourier and wavelet analysis in the context of studying turbulent plasma flows. Fourier modes arise naturally in the study of weak plasma turbulence. Because the full non-linear equations of motion of a plasma (in kinetic and fluid descriptions) are analytically intractable, much analytic work has focused on the linear approximation. For homogeneous plasmas, weak fluctuations are then typically described by normal modes that vary as independent Fourier components $\propto \exp(i\omega t - ikx)$, with a dispersion relation $\omega = \omega(k)$ imposed by the linearized equations of motion. Theories of weak plasma turbulence were developed by treating the non-linear interactions of the normal modes by perturbation theory [13–16]. The complexity of turbulent flows is then ascribed to the interaction of a large number of incoherent Fourier components [17], resulting in a cascade of energy [18] between large scales (low k) and small scales (high k).

While Fourier analysis is thus a natural tool for studying weak turbulence, it may not be well-adapted for characterizing strongly non-linear flows. Strongly turbulent fluid flows include coherent structures such as vortex tubes [19], while magnetized plasma turbulence displays the formation of current sheets [2, 20–22]. In Fourier space, these localized coherent structures require a large number of modes for their description.

To illustrate a limitation of Fourier spectral analysis, two test signals are shown in

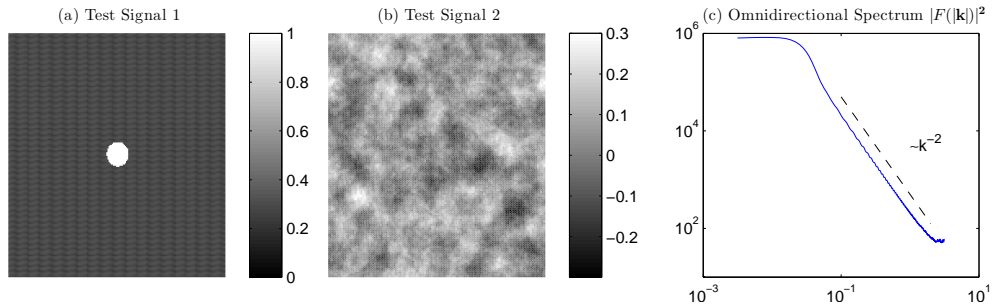


FIG. 1: (a-b) Two test signals have identical (c) Fourier power spectra (these spectra are integrated over angular directions). Fourier modes are spread over space, and the localized structure in (a) therefore consists of coherent contributions from all Fourier modes. **A color table needs to be added.**

Figs. 1(a) and (b) that have identical Fourier power spectra, but their Fourier modes have different phase. In terms of Fourier wave number, each signal exhibits a power-law tail that scales as $|\tilde{F}(k)|^2 \propto 1/|k|^2$. It is apparent, however, that the two signals are qualitatively different. Test Signal 1 in Fig. 1(a) is completely localized peak to a central circle, whereas Test Signal 2 in Fig. 1(b) is spread over space. Because Fourier modes extend over all of space, capturing a localized signal requires coherent contributions from a large number of Fourier modes. As a 1D example, the Heaviside step function, which is discontinuous and defined by

$$\theta(x) = \begin{cases} 0, & \text{if } x \leq 0 \\ 1, & \text{if } x > 0 \end{cases} \quad (1)$$

has Fourier components $\tilde{\theta}(k) = -i/2\pi k$ for $|k| > 0$. The sharp jump in $\theta(x)$ is thus encoded in the coherent phases of its Fourier components, which display a power-law as a function of k , similar to the 2D example of Test Signal 1. By contrast, Test Signal 2's Fourier power spectrum also contains a $1/k^2$ tail, but there is little information contained in the coherence of the phases of the Fourier components. Indeed, Signal 2 was generated by multiplying each Fourier component of Signal 1 by a (pseudo-)random complex phase.

Wavelets, see e.g., [23], provide a different set of basis functions, and they are particularly adapted for capturing localized coherent structures across a range of different scales. Like Fourier modes, certain wavelet families form an ortho-normal basis for decomposing functions of one or more variables. Unlike Fourier modes, however, wavelets are not solutions to

any particular physical equations. Rather, they are constructed to analyze general signals with multi-scale strucure. While Fourier modes capture a single wavelength but are spread out over physical space, wavelets encode localized information about both scale and position.

Several different wavelet families have been derived. Here, we use a discrete "coiflet" basis [24] that gives rise to a multi-resolution [25] representation of 2D functions. The family of wavelets is built out two specially chosen functions: a so-called mother wavelet $\psi(x)$ and a scaling function $\phi(x)$, each of which is plotted in Fig. 2. One key characteristic of the this wavelet function $\psi(x)$ is that it is non-zero over only a finite range. The family of 1D wavelets is given by the translations and dilations of the mother wavelet:

$$\psi_{l,n}(x) = \frac{1}{\sqrt{2^l}} \psi\left(\frac{x - 2^l n}{2^l}\right), \quad (2)$$

where the scale l and shift n each span the integers. Built from these 1D wavelets along with similar translations and dilations of the scaling function ϕ , an ortho-normal basis for 2D functions may be defined by the functions

$$\Psi_{l,m,n}^p(x, y) = \begin{cases} \psi_{l,m}(x)\phi_{l,n}(y), & \text{for } p = H \\ \phi_{l,m}(x)\psi_{l,n}(y), & \text{for } p = V \\ \psi_{l,m}(x)\psi_{l,n}(y), & \text{for } p = D \end{cases} \quad (3)$$

where again l , m , and n span the integers; and p corresponds to three directions typically referred to as *Horizontal*, *Vertical*, and *Diagonal*. In practice for our discrete simulation data, we decompose each signal over a finite number of levels $l < L$ and shifts (which depend on the size of the numerical grid). Up to corrections for boundary cells, each 2D field $F(x, y)$ defined on the compuational grid is de-composed in the wavelet basis as:

$$F(x, y) = \sum_{m \leq N_x, n \leq N_y} A_{m,n} \phi_{L,m}(x)\phi_{L,n}(y) + \sum_{p, l \leq L, m, n} D_{p,l,m,n} \Psi_{l,m,n}^p(x, y), \quad (4)$$

where the coefficients $A_{m,n} = \langle F, \Phi \rangle$ of the expansion give a coarsest level- L approximation of the field, and the wavelet coefficients $D_{c,l,m,n} = \langle F, \Psi \rangle$ retain information on the finer-level details.

III. ITERATIVE WAVELET FILTERING

It has been suggested that turbulence in fluid flows may be characterized by the presence of a strong incoherent portion [4]. The incoherent background acts as a drive, which may

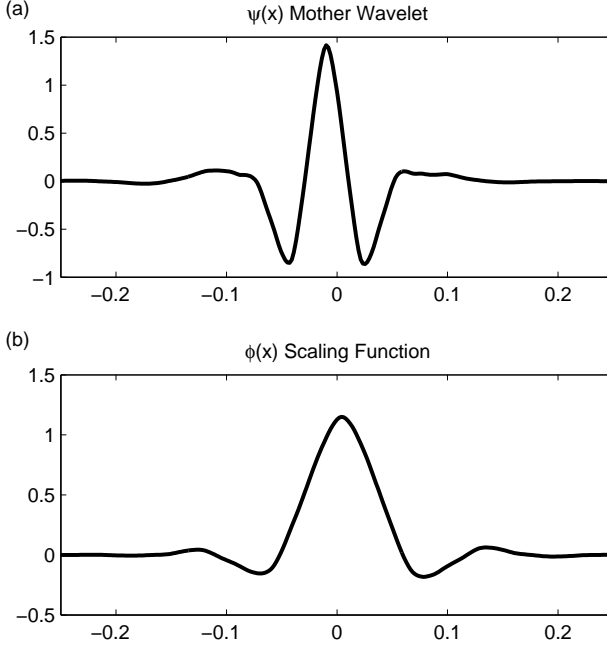


FIG. 2: (a) The mother wavelet of the coiflet-18 wavelet family used in our analysis. (b) The coiflet scaling function.

be modeled as a stochastic forcing term [5], on a collection of coherent structures. Wavelet techniques have been employed to analyze direct numerical simulations [26] as well as serving as a basis for coherent vortex simulations [27].

We apply an iterative wavelet filtering method [26, 28, 29] to the current density from numerical solutions of turbulent plasma flows. The iteration procedure determines an optimal cut-off threshold for the N wavelet coefficients $\{A_{m,n}, D_{p,l,m,n}\}$, which we refer to generically as $\{C_I\}$. Coefficients C_I below the threshold are classified as part of a background of incoherent noise. The coefficients above the threshold contribute to the coherent features of the flow. The incoherent noise is assumed to be additive, Gaussian, and white [27, 30]. The method proceeds as follows:

1. A choice is made of a multiplicative factor α , the number of levels in the wavelet decomposition L , and the wavelet basis. The number of levels L is chosen so that $2^L \sim \min(N_x, N_y)$ where N_x and N_y are the number of computational grid points in each direction of the domain. We discuss the choice of α below.
2. The current density is expressed as a sum over an ortho-normal wavelet basis with N coefficients $\{C_I\} = \{A_{m,n}, D_{p,l,m,n}\}$.

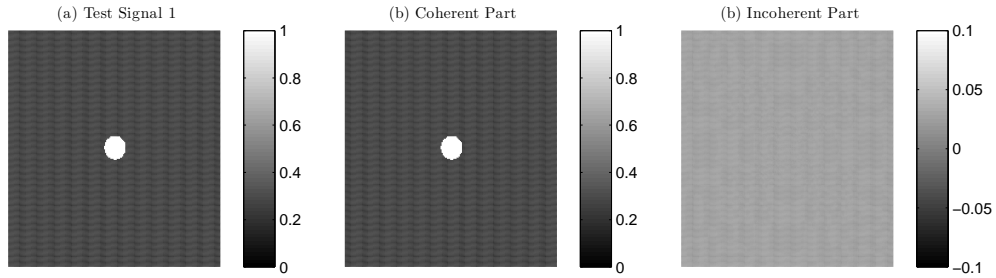


FIG. 3: The iterative wavelet filter is used to decompose Test Signal 1 from Fig. 1(a) into coherent and incoherent parts. The incoherent part is negligible.

3. A threshold $\epsilon = \alpha \sqrt{Var(\{C_I\}) \log(N)}$ is initialized based on the variance of the set of coefficients $\{C_j\}$.
4. The incoherent (or noise) portion of the current density is defined by the coefficients \hat{C}_I , where $\hat{C}_I = C_I$ if $C_I < \epsilon$ and the remaining coefficients $C_I > \epsilon$ are discarded.
5. A new threshold $\epsilon = \alpha \sqrt{Var(\hat{C}_I) \log(N)}$ is computed based on the extraced noise.
6. Steps 4 and 5 are repeated until the threshold ϵ varies less than 5% over an iteration.

In practice, the method typically converges to this tolerance after 2-4 iterations.

To illustrate the effect of the iterative wavelet filter, we apply it to the two test signals of Fig. 1(a-b). The decomposition into coherent and incoherent parts as defined by the wavelet filter are plotted in Figs. 3 and 4, where for both cases we set the parameters $\alpha = 10$ and $L = 8$ and used the coiflet-18 basis [24]. The main conclusions do not depend on the choice of wavelet basis. Nevertheless, it is useful for turbulent flows to choose a basis with a large number of vanishing moments (the coiflet-18 wavelets have six vanishing moments), which tends to cancel the wavelet coefficients in smooth regions free of discontinuities and high-order derivatives [4]. For the localized, coherent Test Signal 1 in Fig. 3, the method finds a practically negligible incoherent noise part. For Test Signal 2 in Fig. 4, a background noise is extracted. Note that the coherent portion of the signal in Fig. 4(b) is reconstructed from only $\sim 0.07\%$ of the wavelet coefficients even though it contains over 99% of the "energy" $\sum_n F_n^2$. This ability to capture a large portion of a signal with a small number of coefficients explains the wide-spread use of wavelets for digital signal compression [31].

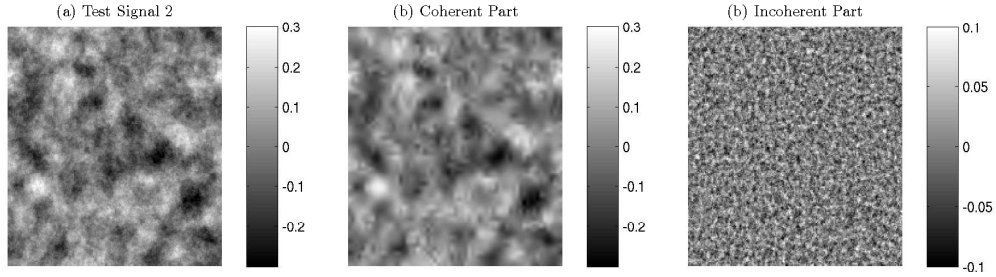


FIG. 4: The iterative wavelet filter is used to decompose Test Signal 2 from Fig. 1(b) into coherent and incoherent parts. The coherent part is represented by only $\sim 0.07\%$ of the wavelet coefficients.

IV. SIMULATION SET-UP

To study the transition to turbulence of a magnetized plasma flow, we consider four different models of Kelvin-Helmholtz unstable flow-shear layers. In each case, the system is doubly periodic in a domain of size $L_x \times L_y = 7.5\pi \times 5\pi d_i$, where d_i is the ion inertial skin depth based on the uniform density n_0 . The initial magnetic field is uniform and mainly out of the simulation plane, $B_z = B_0$, with a small additional in-plane component $B_y = 0.05B_0$. Two flow-shear layers are given with velocity profiles:

$$\frac{v_y(x)}{v_0} = \tanh\left(\frac{x - L_x/4}{\lambda}\right) - \tanh\left(\frac{x - 3L_x/4}{\lambda}\right) - 1, \quad (5)$$

where $v_0 = 0.5v_A = 0.5B_0/\sqrt{4\pi n_0 m_i}$ and the scale length $\lambda = 0.5d_i$. A motional electric field $\mathbf{E}(x) = -\mathbf{v}(x) \times \mathbf{B}$ is also included.

This system is modeled with four different types of plasma simulation methods: (1) fully kinetic particle-in-cell modeling using the codes VPIC [32] and Osiris fonseca:2002, (2) hybrid kinetic ion/fluid electron modeling using the PIC code H3D, (3) two-fluid modeling using the code ... [], and (4) Hall-MHD modeling using the code ... [33]. For each simulation, we focus on only one of the shear-flow layers, in particular whichever layer transitions to a turbulent state the fastest.

Table with numerical parameters...

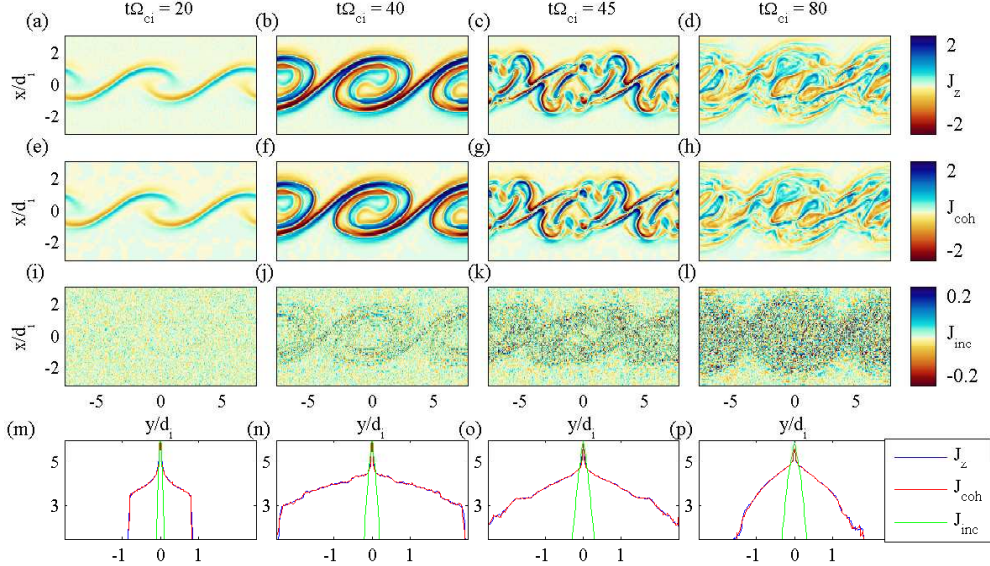


FIG. 5: Fully kinetic PIC results. (a-d) Profiles of the out-of-plane current density J_z over the course of a VPIC simulation. (e-h) The coherent part J_{coh} of J_z extracted through the iterative wavelet filtering. (i-l) The residual incoherent part $J_{inc} = J_z - J_{coh}$. (m-p) PDFs of the total out-of-plane current density J_z (blue), the coherent portion extracted by the wavelet method J_{coh} (red), and the incoherent portion J_{inc} (green).

V. MEASURING THE TRANSITION TO TURBULENCE

Our goal is to test the iterative wavelet filtering method on each of the four types of plasma simulation to determine if the wavelet analysis is capable of identifying the onset of turbulence. While there are differences in the details of the current sheets and flows between the various plasma simulation models, we do not attempt to characterize these differences here. Indeed, a positive feature of wavelet analysis is that it does not pre-suppose a model for the coherent structures that arise in the turbulent flow.

The out-of-plane current density J_z is plotted in Fig. 5(a-d) at four time slices over the course of the high-resolution VPIC simulation with 10,000 particles per cell and 3328×2560 cells. The coherent part of the current J_{coh} extracted through the wavelet method yields the profiles in Figs. 5(e-h). The percentage of wavelet coefficients required to reconstruct the coherent portion ranges from $\sim 0.06\%$ at $t\Omega_{ci} = 20$ to $\sim 0.13\%$ at $t\Omega_{ci} = 80$. Nevertheless, this small fraction of coefficients contains 99% of the “energy” (defined as $\sum J_z^2$) at $t\Omega_{ci} = 20$ and 96% at $t\Omega_{ci} = 80$.

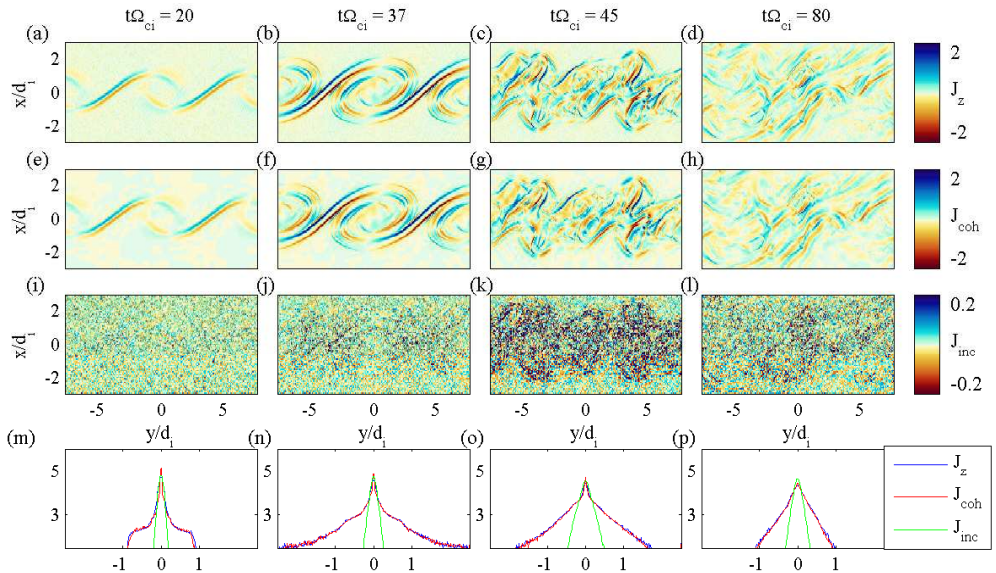


FIG. 6: Hybrid (kinetic ion/fluid electron) PIC simulation results. Similar plots as in Fig. 5.

The logarithm of the probability distribution function (PDF) of values of J_z over the entire simulation domain is plotted for each time slice in Figs. 5(m-p). The wavelet filtering technique extracts a large coherent portion of each current density profile. These coherent piece contains slowly decaying PDFs, which are approximately power laws for a range of values. The coherent portion of the current density thus includes intermittent current sheets, which have been identified as key sites of dissipation in kinetic turbulence [1, 2]. The incoherent portion (green curves) is nearly Gaussian noise, corresponding to parabolic profiles in the logarithmic plots. Similar plots from each of the simulations are shown in Figs. 6-8.

To study the transition to turbulence as the initial laminar Kelvin-Helmholtz vortices break apart into smaller structures and generate dissipation-scale current sheets, we plot the norm, defined as $|J| = \sqrt{\sum J^2}$, of the total current density $|J_z|$ and the incoherent part $|J_{inc}|$ over time for each simulation in Fig. 9. In each case, the total current density norm $|J_z|$ increases as the Kelvin-Helmholtz vortex forms. Even when the vortex reaches a non-linear state near the maximum of $|J_z|$, the incoherent part $|J_{inc}|$ remains small. The incoherent part $|J_{inc}|$ then undergoes a relatively rapid increase in magnitude as the vortex breaks apart through turbulent motions and generates current sheets over a range of length scales. We associate this rapid increase and subsequent saturation of the incoherent part $|J_{inc}|$ with the onset of turbulence.

We note that it is difficult to characterize this onset of turbulence based only on Fourier

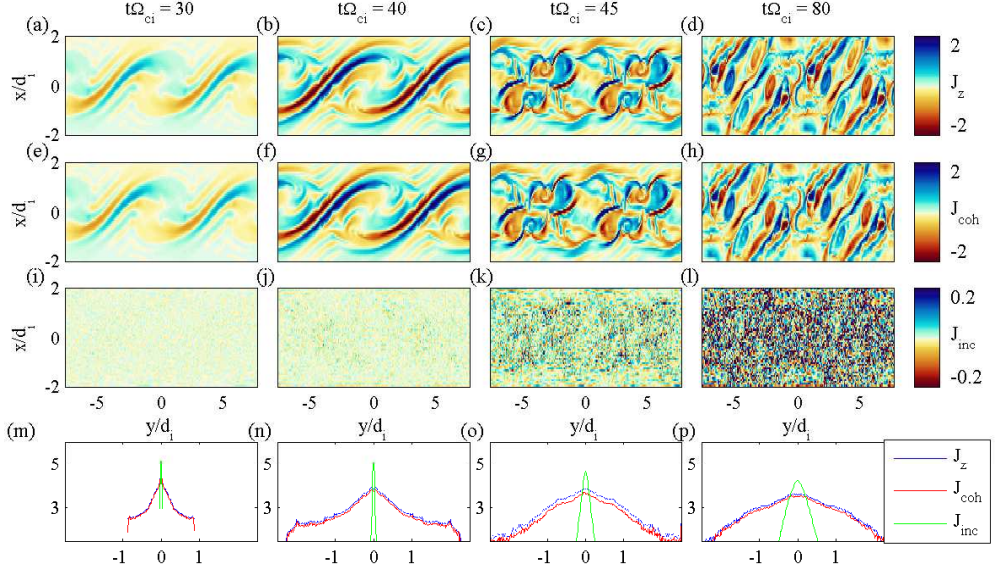


FIG. 7: Two-fluid simulation results. Similar plots as in Fig. 5.

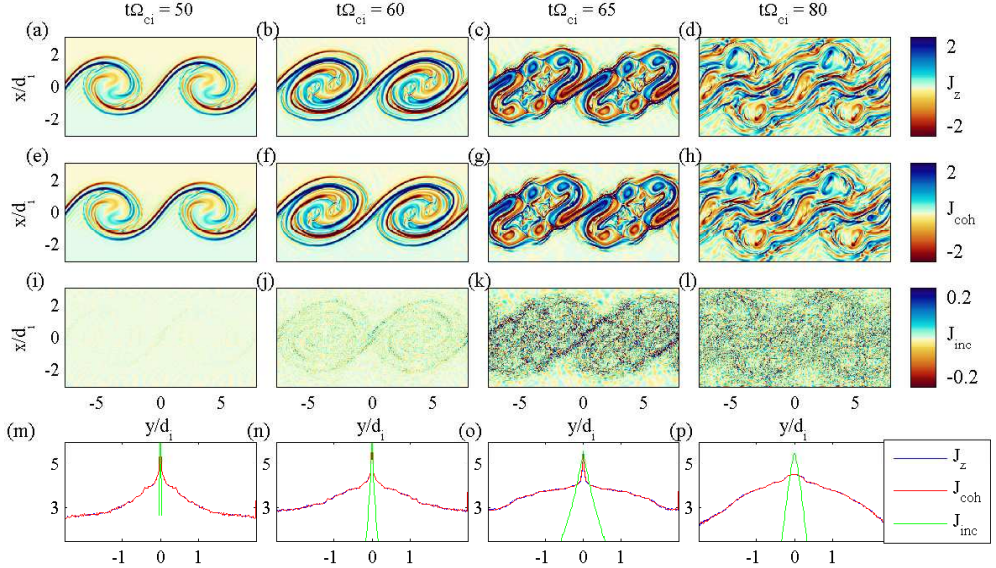


FIG. 8: Hall MHD simulation results. Similar plots as in Fig. 5.

spectral data. To illustrate this, the Fourier power spectra of the current density from the fully kinetic simulation at early ($t = 25/\Omega_{ci}$) and late ($t = 80/\Omega_{ci}$) time are plotted in Fig. 10. The late-time, turbulent time slice (black) does have a stronger signal at somewhat larger k and has overall greater energy than the early-time, laminar time slice (red). Nevertheless, the two power spectra have very similar shapes and slopes, with no clear indication that the later time is turbulent.

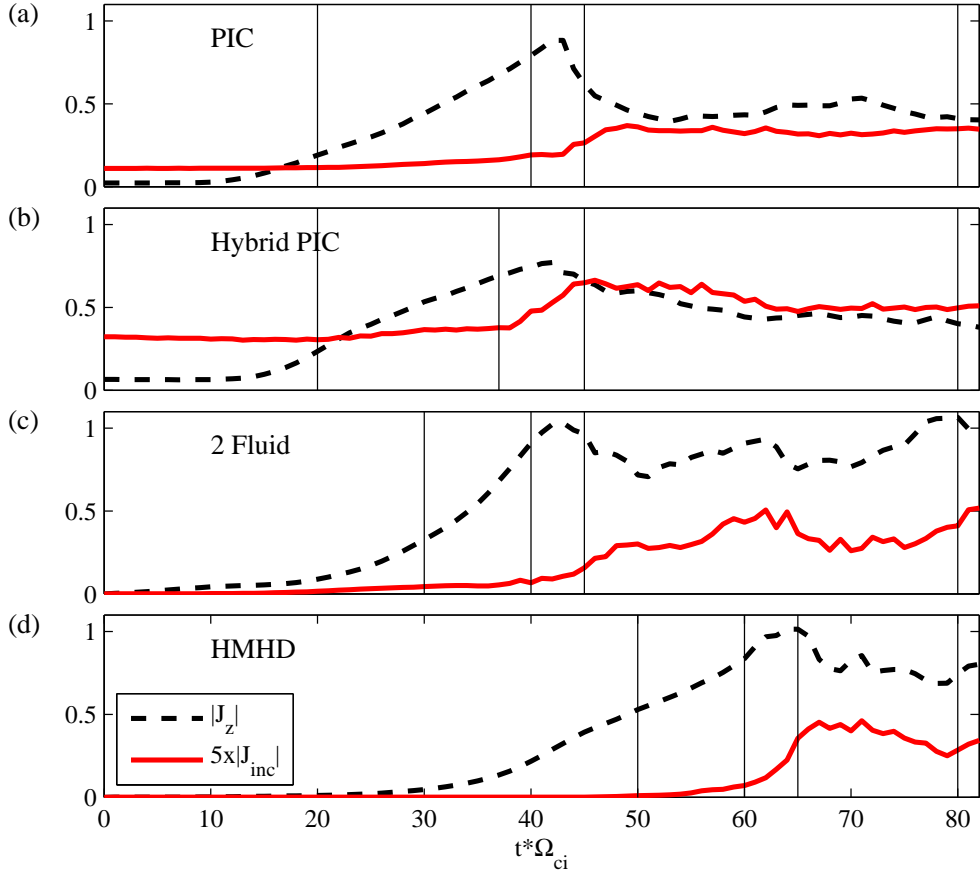


FIG. 9: The norm of the current density, $|J| = \sqrt{\int |J(x, y)|^2 dx dy}$, over the simulation domain of the total out-of-plane current J_z (black) and the incoherent portion J_{inc} (red, scaled by a factor of 5) are plotted over time for (a) the fully kinetic PIC simulation, (b) the hybrid PIC simulation, (c) the two-fluid simulation, and (d) the Hall MHD simulations. In each plot, the vertical lines indicate the time steps used in Figs. 5–8. The incoherent part increases and then saturates as the dynamics become turbulent.

VI. TURBULENCE IN A GLOBAL MAGNETOSPHERE SIMULATION

In this section, we apply the wavelet techniques described above to analyze turbulence in a 2D hybrid global magnetosphere model produced with the code H3D [34]. The model consists of a fixed dipolar magnetic field (enclosed in a conducting spherical "planet") and a solar wind entering the simulation from the left with an Alfvén Mach number of 8. The domain is 4096×2048 cells with 200 particles per cell. A bow shock forms where the flow collides with the planetary magnetic field. Behind the bow shock is the magnetosheath,

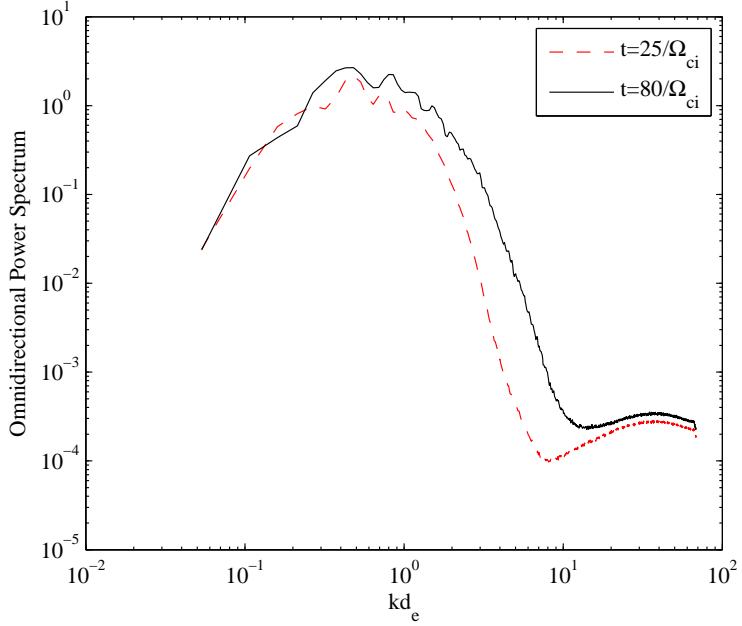


FIG. 10: Fourier spectra of J_z from the fully kinetic VPIC simulation at early time $t = 25/\Omega_{ci}$ (red) before the onset of turbulence and late time $t = 80/\Omega_{ci}$ (black) after turbulence has fully developed.

which is an often turbulent layer of shocked solar wind plasma separated from the planetary dipole field by an inner boundary layer called the magnetopause. The kinetic simulation resolves the formation of the ion foreshock, an extended region upstream of the bow shock driven by beams of ions reflected from the shock. The foreshock instabilities are strongest and most spatially extended along magnetic field lines that are quasi-parallel to the shock normal. The foreshock fluctuations steepen and develop into turbulence and coherent jets when they are convected into the magnetosheath.

In this simulation, a rotational discontinuity was launched in the solar wind. The corresponding sharp rotation of the magnetic field direction is visible in Fig. 11(a). As the discontinuity crosses the planetary magnetosphere, the region where the magnetic field is quasi-parallel to the shock normal changes. As a result, the strongest foreshock and magnetosheath fluctuations move from the northern hemisphere to the southern hemisphere (compare Figs. 11(a) and (d) for example). We consider here whether the wavelet analysis techniques offer a means of quantifying this localized shift of the turbulent flow features in this highly inhomogeneous system.

In Fig. ??(a), we plot the coherent part B_{coh} of the fluctuations of the magnetic field

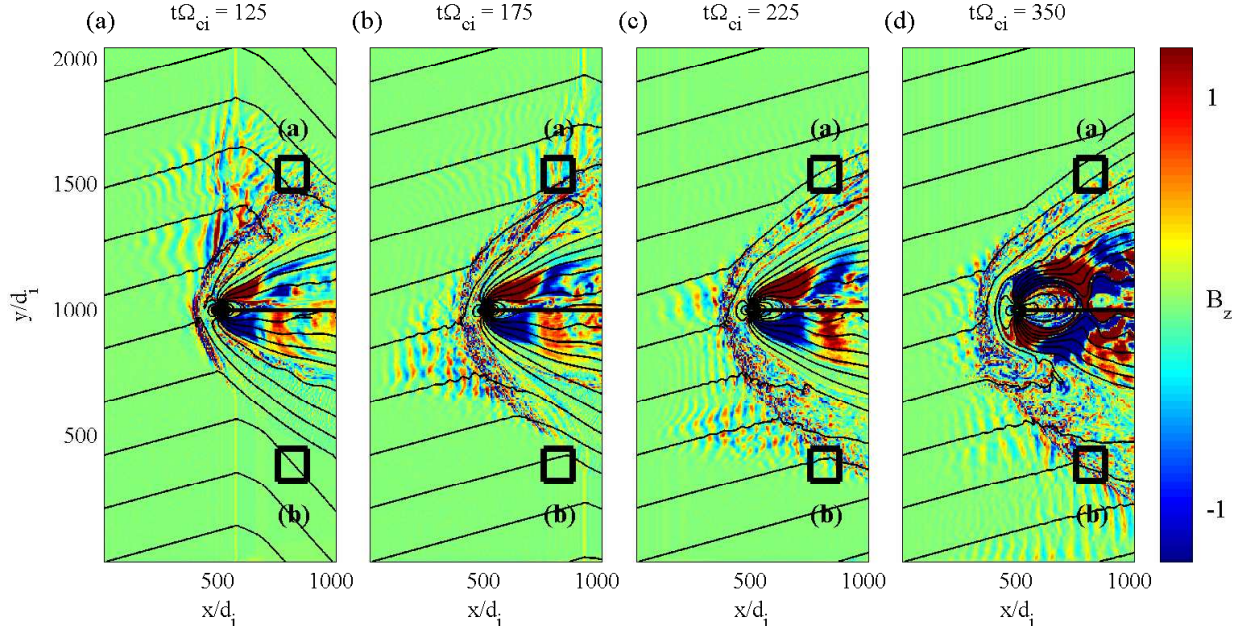


FIG. 11: The magnetic field component B_z out of the simulation plane from four time steps of a hybrid global magnetosphere simulation. A rotational discontinuity is launched in the solar wind, and it is visible in (a) at $x \sim 1000d_i$. The boxes indicate the regions where localized turbulence is analyzed in Fig. 13.

component B_z out of the simulation plane, extracted using the iterative wavelet filter. The incoherent part $B_{inc} = B_z - B_{coh}$ is then used to locate regions of turbulence. The absolute value of the incoherent part is smoothed with a Gaussian filter with a width of ~ 80 cells, as plotted in Fig. 12(b). Following the results of the analysis of Kelvin-Helmholtz unstable flows of Sec. V, we identify the turbulent regions as those with a large incoherent signal. Selecting a threshold of $|B_{inc}| = 0.15B_0$ produces the magenta contours plotted in Figs. 12(a) and (b), and these contours thus contain the turbulent regions as defined using the wavelet analysis technique.

To illustrate the change of the turbulent regions over time, we analyze the flows within two small sub-domains of the simulation. These two sub-domains are the 256-cell wide squares plotted in Figs. 11 and 12. The magnetic field B_z within each square is de-composed into coherent and incoherent parts over the course of the simulation, and the norms of the signals are plotted in Fig. 13. For box (a), the development of turbulence in similar to the Kelvin-Helmholtz unstable flows analyzed previously: a relatively strong coherent signal develops

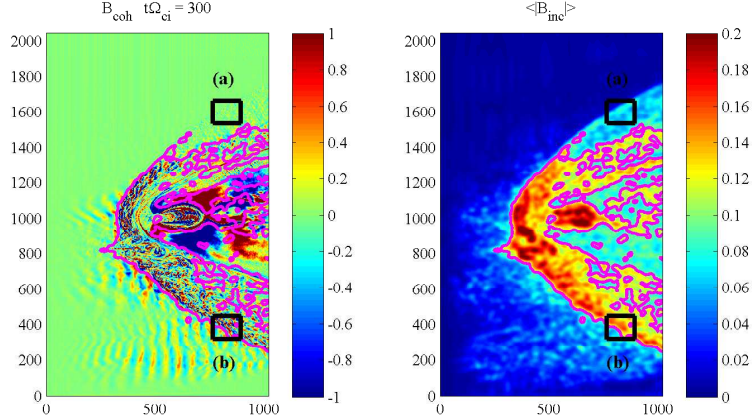


FIG. 12: The iterative wavelet method applied to the global simulation extracts a coherent part plotted in (a). In (b), the absolute value of the incoherent part is smoothed over ~ 80 cells. Turbulence is associated with regions containing a large incoherent signal, with the magenta contour indicating a level of $0.15 B_0$. The boxes indicate the regions where localized turbulence is analyzed in Fig. 13.

early (*e.g.*, at $t = 125/\Omega_{ci}$), and the incoherent or turbulent feature grows shortly thereafter.

After the rotational discontinuity in the solar wind crosses the planet, the region of turbulence moves towards the southern hemisphere where the magnetic field is quasi-parallel to the shock. For box (b), the transition to turbulence is different from box (a). Because of the background solar wind flow, turbulent fluctuations are advected into box (b) even before large coherent waves develop (*e.g.*, at $t = 200/\Omega_{ci}$). This highlights that in systems with non-local drives and strong convective contributions such as the foreshock (which derives its free energy from particles reflected from a faraway shock and is embedded in a high-speed solar wind flow), the transition to turbulence need not follow the precise pattern found in the somewhat simpler sheared flow layers. The sheared flow layers exhibited a classical cascade from the large scales of the global flow to more and smaller scales as turbulence developed locally. In real data, however, turbulent fluctuations at a given spatial location may precede in time the observation of large coherent structures.

VII. SUMMARY

An iterative wavelet filtering technique was applied to a set of simulations of Kelvin–Helmholtz unstable plasma flows to separate the current density into coherent and incoherent

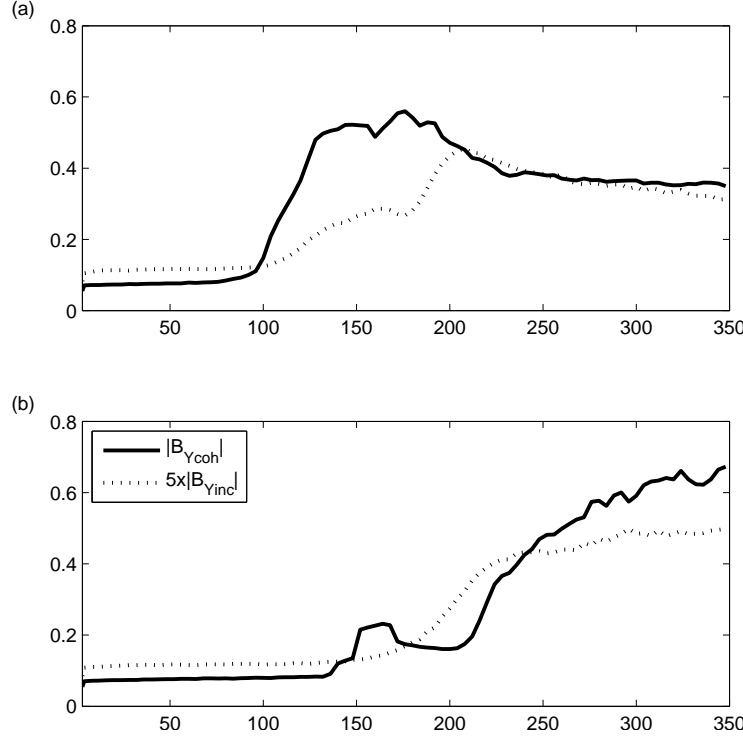


FIG. 13: The magnetic field component B_z out of the simulation plane from four time steps of a hybrid global magnetosphere simulation.

pieces. The onset of turbulence over time was identified by a sharp increase in magnitude of the incoherent background.

Acknowledgments

A.L. was supported by the LDRD office at LANL...Pleiades provided by NASA's HEC Program. K.S. acknowledges support by the French Research Federation for Fusion Studies carried out within the framework of the European Fusion Development Agreement (EFDA).

Appendix: Noise in Particle Simulations

For the fully kinetic PIC simulation and the hybrid PIC simulation in Figs. 9(a-b), the incoherent piece of the current density has non-negligible norm even at the beginning of the simulations. This offset of the incoherent piece is produced not by some initially imposed level of turbulence, but rather by the presence of numerical noise associated with the PIC

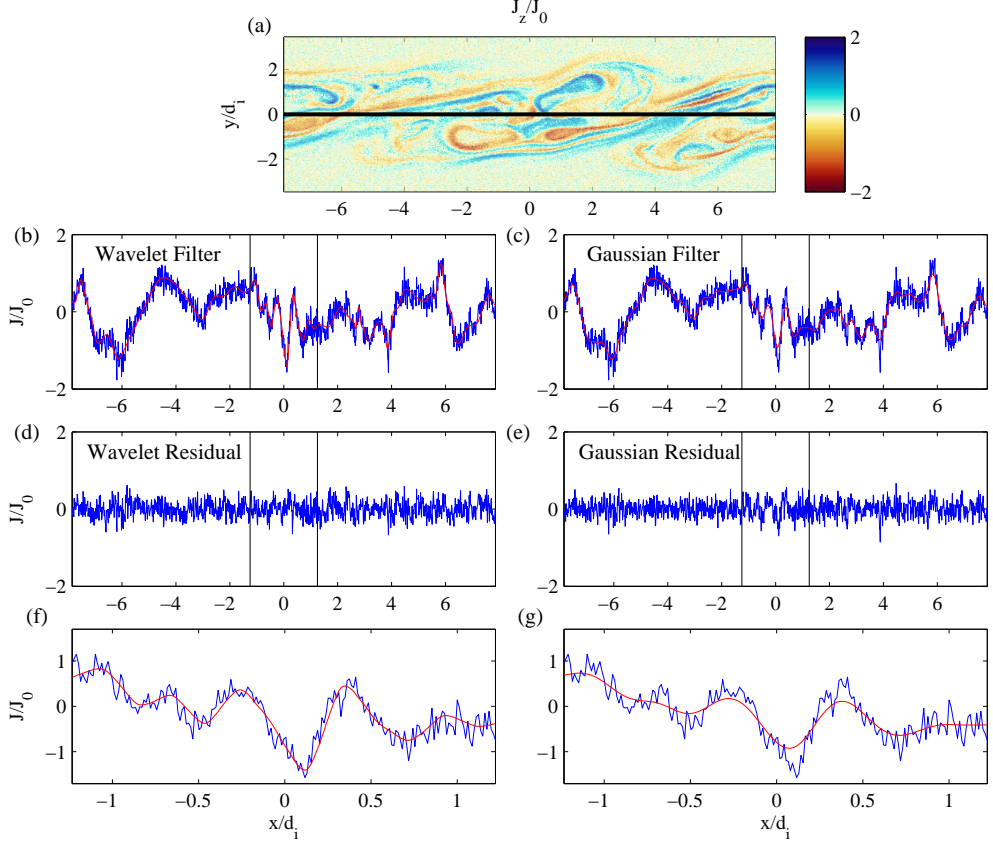


FIG. 14: (a) The out-of-plane current density J_z from the VPIC fully kinetic simulation with 150 particles per cell per species. The current density along the horizontal cut in (a) is plotted in blue along with filtered data in red based on (b) an iterative wavelet filter and (c) a Gaussian filter. (d-e) Show the residuals (current density minus filtered data). (f-g) Plots zooming in on the region delineated by vertical lines in (b-e). Note that the wavelet filter tends to maintain peak values in current sheets on electron scales, while a Gaussian filter tends to smooth these out.

method. In PIC kinetic modeling, which samples phase space with a finite number of numerical macro-particles, there is statistical numerical noise $\propto 1/\sqrt{N_p}$, where N_p is the number of macro-particles in each grid cell of the domain. The particle noise results from statistical fluctuations in the number of particles in each cell, and it therefore has spatial features on the scale of the grid. Below, we explore the use of wavelet filtering for de-noising particle simulations and compare it to other smoothing algorithms. A detailed study of wavelet-based denoising for density estimation can be found in [9].

The out-of-plane current density J_z plotted in *Fig. 14(a)* is computed from summing the

contributions from particles in each cell of the simulation, which in this case was initialized with 150 particles per cell. The grid-scale numerical noise is apparent. In Fig. 14, two methods for filtering the grid-scale statistical noise for a PIC simulation are compared. The first is the wavelet filter applied above to study coherent turbulent structures. The only difference is that a value of the multiplicative factor $\alpha = 1$ is used. The second filtering method is a classical low-pass Gaussian filter, which convolves the signal with a Gaussian kernel. A cut of J_z along the center at $y = 0$ is plotted (in blue) in Figs. 14 (b) and (c) along with 1D filtered data (in red). The wavelet filtered data \tilde{J}_z was obtained using the iterative method described above. The residual noise, $J_z - \tilde{J}_z$, is plotted in Fig. 14 (d). The width of the Gaussian filter, $\sigma \sim 6$ cells, in Fig. 14(c) was chosen so that the noise extracted (the residuals) in Figs. 14(d) and (e) have the same energy norm.

The wavelet filter and the Gaussian filter result in similar de-noised signals. The largest differences between the two filtering methods occur at narrow current sheets. Figures 14(f) and (g) zoom in on the regions between the vertical lines in Figs. 14(b-e). A main advantage of the wavelet filtering method is that it better preserves the peak values of sharp features in the current profile. By design, the wavelet basis captures significant features at any scale. The Gaussian filter (or similarly any low-pass band filter), on the other hand, preferentially smooths out small-scale features. The peak values of the current density in the thin sheets in this region are therefore substantially reduced by the Gaussian filter.

The wavelet and Gaussian filtering provide means of de-noising by post-processing the PIC data after a run. We compare the effect of de-noising through post-processing to runtime methods that are intrinsically less noisy. One method of reducing noise is simply to increase the number of particles in the simulation, which results in smaller statistical noise $\propto 1/\sqrt{N_p}$ but increased computational cost. In Fig. 15, we include a spectrum of magnetic fluctuations from a higher-resolution VPIC simulation with 10,000 particles per cell. The spectrum may be compared to the lower-resolution VPIC run with 150 particles per cell, as well as data from the lower-resolution run de-noised with either a Gaussian filter or the iterative wavelet technique. For the unfiltered data, the spectra turn upwards at large $k d_e > 5$, which corresponds to roughly the grid scale. The higher-resolution simulation with 10,000 particles per cell has reduced noise, and the portion of the spectrum unaffected by particle noise extends to higher k than in the case with only 150 particles per cell.

Another method of reducing the noise levels in PIC simulations is to employ high-order

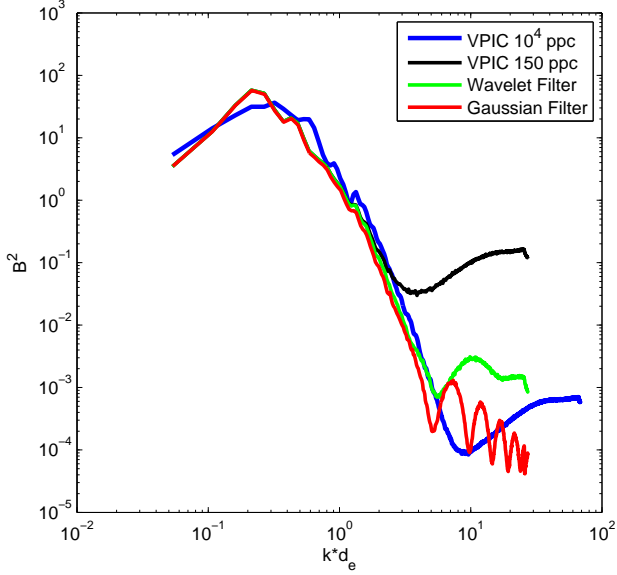


FIG. 15: A wavelet filter and a low-pass Gaussian filter were used to remove particle noise from a VPIC simulation with 150 particles per cell. The resulting magnetic field spectra are compared to a high-resolution VPIC run with 10,000 particles per cell.

particle form factors, which smooth and deposit the macro-particle charges and currents over a region larger than one cell [35]. Although this method comes at an increased computational cost for each numerical particle push, it can substantially reduce the level of noise in the simulation. Figure 16 compares magnetic fluctuation spectra from fully kinetic VPIC runs with 150 and 10,000 particles per cell (same runs as Fig. 15) to fully kinetic runs using various smoothing and higher-order particle shapes with the code OSIRIS.

- [1] M. Wan, W. H. Matthaeus, H. Karimabadi, V. Roytershteyn, M. Shay, P. Wu, W. Daughton, B. Loring, and S. C. Chapman, Phys. Rev. Lett. **109**, 195001 (2012), URL <https://link.aps.org/doi/10.1103/PhysRevLett.109.195001>.
- [2] H. Karimabadi, V. Roytershteyn, M. Wan, W. Matthaeus, W. Daughton, P. Wu, M. Shay, B. Loring, J. Borovsky, E. Leonardis, et al., Physics of Plasmas **20**, 012303 (2013).
- [3] A. Grossmann and J. Morlet, SIAM journal on mathematical analysis **15**, 723 (1984).
- [4] M. Farge, Annual review of fluid mechanics **24**, 395 (1992).
- [5] K. Schneider and O. Vasilyev, Annual Review Fluid Mechanics pp. 473–503 (2010).

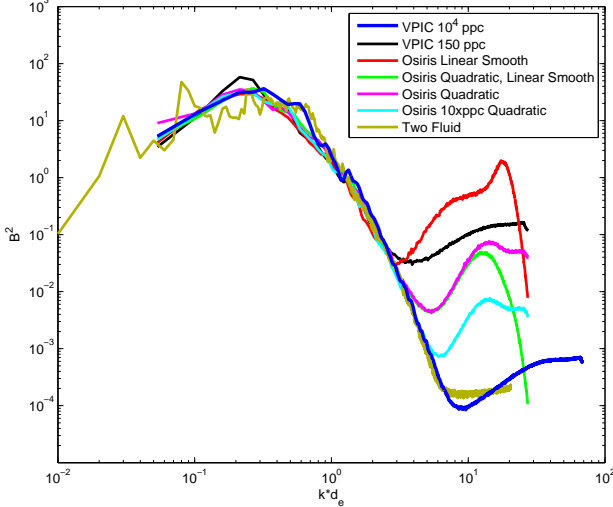


FIG. 16: The omni-directional power spectrum of the magnetic field $|\mathbf{B}(k)|^2$ from various simulation runs.

- [6] T. Dudok de Wit and V. Krasnosel'skikh, Physics of Plasmas **2**, 4307 (1995).
- [7] Z. Vörös, W. Baumjohann, R. Nakamura, A. Runov, M. Volwerk, T. Zhang, and A. Balogh, Physics of Plasmas **11**, 1333 (2004).
- [8] B. P. Van Milligen, C. Hidalgo, and E. Sanchez, Physical review letters **74**, 395 (1995).
- [9] R. Nguyen van yen, D. del Castillo-Negrete, K. Schneider, M. Farge, and G. Chen, Journal of Computational Physics **229**, 28212839 (2010).
- [10] R. Nguyen van yen, E. Sonnendrücker, K. Schneider, and M. Farge, ESAIM: Proceedings **32**, 134 (2011).
- [11] R. Nguyen van yen, N. Fedorczak, F. Brochard, G. Bonhomme, K. Schneider, M. Farge, and P. Monier-Garbet, Nuclear Fusion **52**, 013005 (2012).
- [12] M. Farge and K. Schneider, Journal of Plasma Physics **81**, 435810602 (2015).
- [13] P. A. Sturrock, Proc. R. Soc. Lond. A **242**, 277 (1957).
- [14] A. Galeev, V. Karpman, and R. Sagdeev, Nuclear Fusion **5**, 20 (1965).
- [15] C. Kennel and F. Engelmann, The Physics of Fluids **9**, 2377 (1966).
- [16] S. Galtier, S. Nazarenko, A. C. Newell, and A. Pouquet, Journal of Plasma Physics **63**, 447 (2000).
- [17] P. Manneville, in *Chaos: The Interplay Between Stochastic and Deterministic Behaviour* (Springer, 1995), pp. 257–272.

- [18] A. N. Kolmogorov, in *Dokl. Akad. Nauk SSSR* (1941), vol. 30, pp. 299–303.
- [19] M. Farge, G. Pellegrino, and K. Schneider, Physical Review Letters **87**, 054501 (2001).
- [20] H. Politano, A. Pouquet, and P. Sulem, Physics of Plasmas **2**, 2931 (1995).
- [21] J. TenBarge and G. Howes, The Astrophysical Journal Letters **771**, L27 (2013).
- [22] V. Zhdankin, D. A. Uzdensky, J. C. Perez, and S. Boldyrev, The Astrophysical Journal **771**, 124 (2013).
- [23] S. G. Mallat, IEEE transactions on pattern analysis and machine intelligence **11**, 674 (1989).
- [24] I. Daubechies, SIAM Journal on Mathematical Analysis **24**, 499 (1993).
- [25] B. Jawerth and W. Sweldens, SIAM review **36**, 377 (1994).
- [26] M. Farge, K. Schneider, and N. Kevlahan, Physics of Fluids **11**, 2187 (1999).
- [27] K. Schneider, J. Ziuber, M. Farge, and A. Azzalini, Journal of Turbulence p. N44 (2006).
- [28] D. L. Donoho and J. M. Johnstone, biometrika **81**, 425 (1994).
- [29] A. Azzalini, M. Farge, and K. Schneider, Applied and Computational Harmonic Analysis **18**, 177 (2005).
- [30] N. Okamoto, K. Yoshimatsu, K. Schneider, M. Farge, and Y. Kaneda, Physics of Fluids **19**, 115109 (2007).
- [31] S. G. Chang, B. Yu, and M. Vetterli, IEEE transactions on image processing **9**, 1532 (2000).
- [32] K. J. Bowers, B. J. Albright, L. Yin, B. Bergen, and T. J. T. Kwan, Physics of Plasmas **15**, 055703 (pages 7) (2008), URL <http://link.aip.org/link/?PHP/15/055703/1>.
- [33] L. Chacon and A. Stanier, Journal of Computational Physics **326**, 763 (2016).
- [34] H. Karimabadi, V. Roytershteyn, H. Vu, Y. Omelchenko, J. Scudder, W. Daughton, A. Dimmock, K. Nykyri, M. Wan, D. Sibeck, et al., Physics of Plasmas **21**, 062308 (2014).
- [35] T. Z. Esirkepov, Computer Physics Communications **135**, 144 (2001).